

# Supporting Information

## Subamorphous thermal conductivity of crystalline half-Heusler superlattices

E. Chavez-Angel<sup>1,\*</sup>,<sup>†</sup>, N. Reuter<sup>1\*</sup>, P. Komar<sup>1,2,‡</sup>, S. Heinz<sup>1,2</sup>, U. Kolb<sup>3,4</sup>, H.-J. Kleebe<sup>4</sup> and G. Jakob<sup>1,2</sup>

<sup>1</sup> Institut für Physik, Johannes Gutenberg Universität Mainz, Staudingerweg 7, 55128 Mainz, Germany.

<sup>2</sup> Graduate School Materials Science in Mainz, Staudingerweg 9, 55128 Mainz, Germany

<sup>3</sup> Institute of Inorganic and Analytical Chemistry, Johannes Gutenberg Universität Mainz, Duesbergweg 10-14, 55128 Mainz, Germany.

<sup>4</sup> Institute of Applied Geosciences, TU Darmstadt, Schnittspahnstraße 9, 64287 Darmstadt, Germany.

E-mail corresponding author: [emigdio.chavez@icn2.cat](mailto:emigdio.chavez@icn2.cat)

Keywords: Ultralow thermal conductivity, superlattices, amorphous limit of thermal conductivity

## Nomenclature

<i>a</i>	Lattice constant [m]	<b>Greek symbols</b>	
AC	Alternating current	$\delta$	Error deviation
AFM	Atomic force microscopy	$\phi$	Phase lag
<i>b</i>	Half width of three-omega heater [m]	$\eta$	Surface roughness [nm]
<i>d</i>	Thickness of sample or distance to the centre of the cathode [m]	$\Lambda$	Phonon mean free path [m]
DC	Direct current	$\lambda$	Thermal wavelength and/or wavelength of the heat carrier [m]
<i>f</i>	Frequency [Hz]	$\Theta_D$	Debye temperature [K]
<i>h</i>	Planck constant [J s]	$\omega$	Angular frequency ( $2\pi f$ ) [rad s <sup>-1</sup> ]
<i>i</i>	Imaginary number		
<i>I</i>	Current [A]	<b>Subscripts</b>	
<i>k</i>	Thermal conductivity [W K <sup>-1</sup> m <sup>-1</sup> ]	<i>app</i>	Applied current [A]
<i>k<sub>B</sub></i>	Boltzmann constant [J K <sup>-1</sup> ]	<i>c</i>	Corrected temperature
<i>l</i>	Heater length [m]	<i>iso</i>	Insolation layer
MFP	Mean free path	<i>f</i>	Thin film
<i>N</i>	Number of periods	<i>h</i>	heater
<i>n</i>	Number density of atoms [m <sup>-3</sup> ]	<i>L</i>	Longitudinal polarization
P	Power [W]	<i>r</i>	Reference film
p	Pressure [mbar]	<i>rel</i>	Relative error deviation
<i>R</i>	Resistance [ $\Omega$ ]	<i>rms</i>	Root mean square
<i>SL</i>	Superlattice	<i>S</i>	Substrate
<i>T</i>	Temperature [K]	<i>SLs</i>	Superlattices
<i>U</i>	Voltage [V]	<i>sys</i>	Full system including insulation layer, film of interest, reference and the substrate
<i>v</i>	Sound velocity [m s <sup>-1</sup> ]	<i>T</i>	Transverse polarization
XRR	X-ray reflectivity		

---

\* Equally contributing authors

### Current address

<sup>†</sup> Catalan Institute of Nanoscience and Nanotechnology (ICN2), CSIC and BIST, Campus UAB, Bellaterra, 08193 Barcelona, Spain.

<sup>‡</sup> Photonics Group, Institute of Physics, Lodz University of Technology, Wólczańska 219, 90-924 Łódź, Poland.

# Supporting Information

## Characterization techniques

For structural characterization we employed Cs corrected scanning transmission electron microscope (STEM), X-ray diffraction (XRD) and atomic force microscopy (AFM). The high resolution STEM (HR-STEM) measurements were performed on tripod polished samples using JEOL JEM ARM 200F operated at 200 kV, applying high angle annular dark field (HAADF) imaging. The crystallographic quality was determined based on  $\theta-2\theta$  patterns and  $\omega$  (rocking curve) scans recorded by a Bruker D8 Discovery X-ray diffractometer operated in Bragg-Brentano geometry. Surface roughness was measured by the root mean square (RMS) of a two dimensional power spectral density plot in a representative range of the sample's surface. It was recorded by Veeco Dimension 3100 setup, operated in the contact mode. The samples thickness were measured by using the same AFM equipment.

## 1. Fabrication process

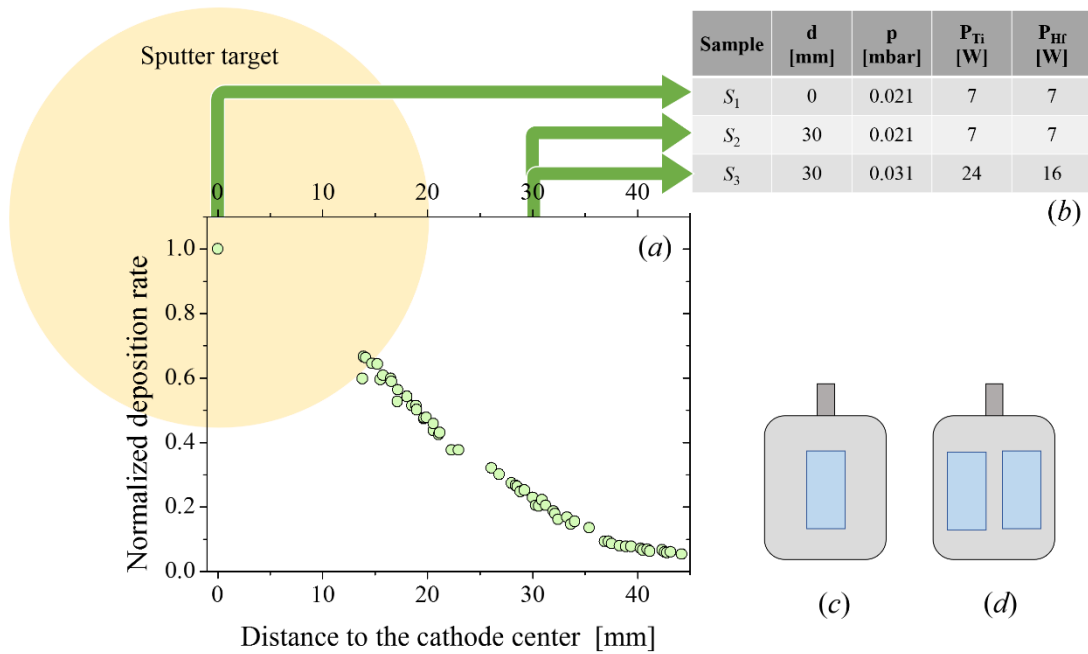


**Figure S1** (a) Normalized deposition rate of the used TiNiSn and HfNiSn cathodes as a function of distance between cathode center line and MgO substrate center (b) The creation parameters for each of the three samples. (c)-(d) Sample holder for a single (c) and double (d) SL deposition.

The SLs were grown by DC magnetron sputtering processes on 10 mm×5 mm MgO substrates using a Vanadium (5 nm) and HfNiSn (25 nm) as a buffer layer at  $T = 520$  °C. The deposition rate was measured using AFM and XRR. As it is displayed in Figure S1, the deposition rate depends on the distance between substrate and central axis of the cathode due to the spiral trajectories that the ionized gas atoms follow around the field lines of the inhomogeneous magnetic field during the sputtering process. The SLs were grown at two different positions in relation to the centre of the cathode using different gas pressure, cathode powers and sample holders.

## Supporting Information

The first sample ( $S_1$ ) was grown above the cathode centre at low Ar pressure ( $p = 0.21$  mbar), low cathode powers ( $P_{\text{Ti}} = P_{\text{Hf}} = 7$  W) and using a single sample holder (see **Figure S1 c**). The second sample ( $S_2$ ) was deposited using the same growing conditions but 30 mm away from the centre of the cathode. The third sample ( $S_3$ ) was grown at the same place of  $S_2$  but with higher Ar pressure ( $p = 0.21$  mbar) and cathode power ( $P_{\text{Ti}} = 24$  W and  $P_{\text{Hf}} = 16$  W). For these three samples ( $S_1$ - $S_3$ ), we kept constant the total number of periods  $N = 37$ . Other two samples were also grown using the same deposition condition than  $S_3$  but with different number of periods  $N = 111$  ( $S_4$ ) and 148 ( $S_5$ ), respectively. In addition, other two samples were grown using the same deposition condition of  $S_3$  but with a different sample holder allowing to place two substrates at the same time (see **Figure S1 d**). As one can see in the **Figure S2**, if we use the double sample holder it is clear to see that one of the substrate we will a little bit closer to one of the cathode. The thickness of all the samples presented in this work was measured by using AFM. A summary of the growth conditions is displayed in the **Table S1**.

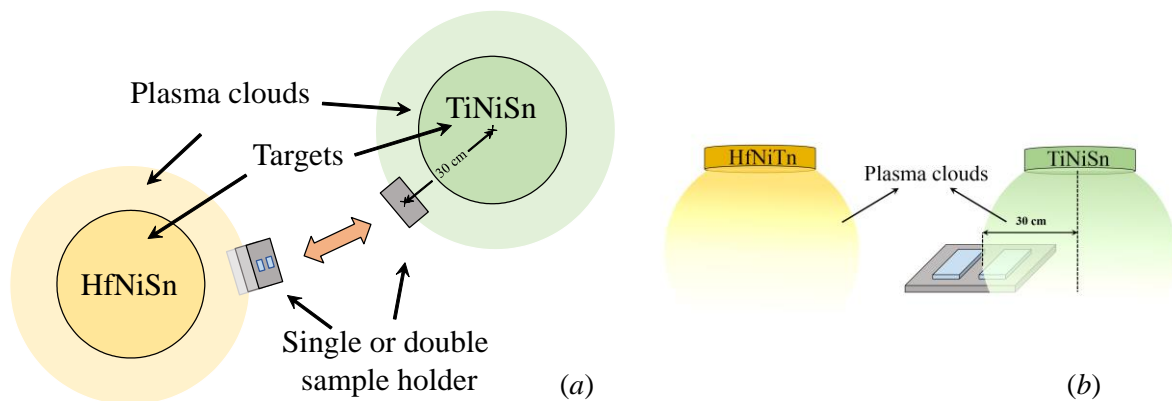


**Figure S2 (a) and (b)** schematic view of the sample deposition and the growth in the inhomogeneous part of the plasma cloud.

### 1.1 Surface and crystal structure analysis

By looking at the AFM surface scans, displayed in **Figure S3 g to i**, one can notice a remarkable difference between the samples at a microscopic scale. Clearly, the samples grown 30 mm away from the cathode are rougher than the ones grown when the sample holder was centred. Additionally, the gas pressure and the power applied to the cathodes have also an impact on the increase of the surface roughness of the samples, as it is shown in the **Figure S3 i**.

Regarding the XRD analysis,  $S_1$  shows satellite peaks that are characteristic for SLs as shown in **Figure S3 a**. The satellite peaks of  $S_2$  and  $S_3$  are less pronounced and less symmetric as expected for samples that were sputtered at a place with spatially inhomogeneous deposition rates leading to unclear interfaces (see **Figure S3 b and c**, respectively). Consequently, the samples are definitely different in the SL structure. However, the crystal quality of all samples is similar as one can see in the Full-Width-Half-Maximum (FWHM) of rocking curves (**Figure S3 d to f**).

## Supporting Information

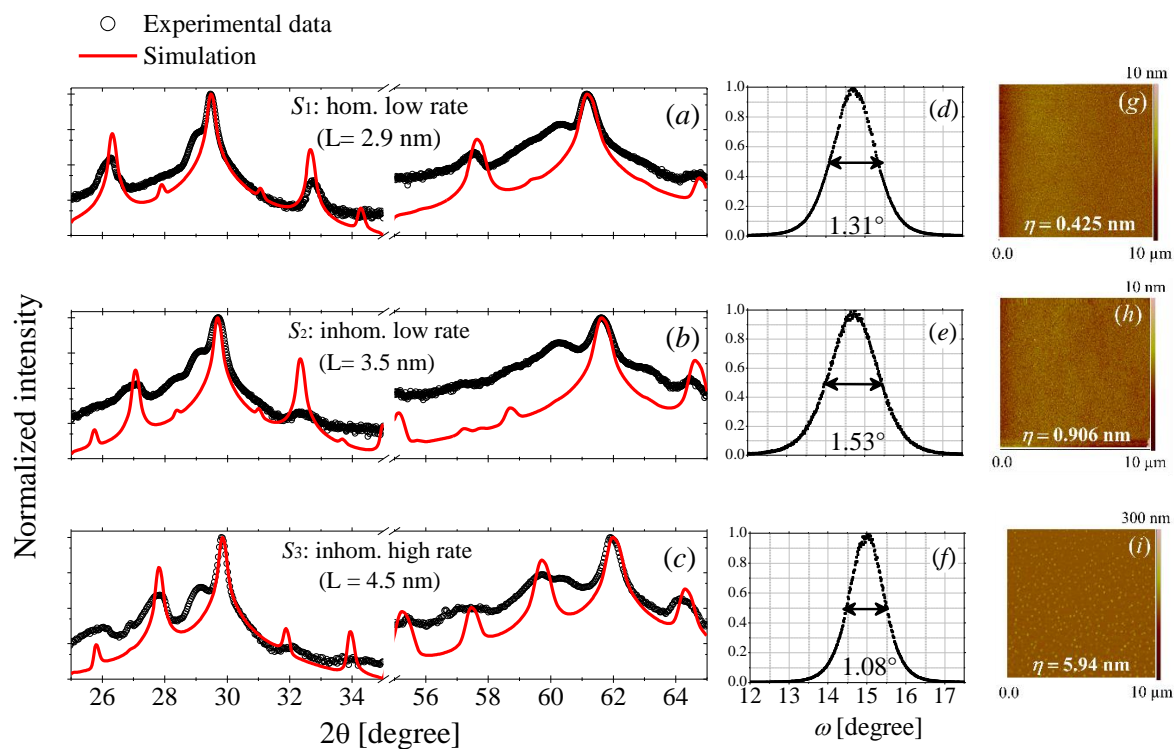


**Figure S3** XRD diffractograms (a) to (c), rocking curves (d) to (f) and AFM surface scans (g) to (i) of 37 periods half-Heusler SLs grown under different deposition conditions. The calculation of the XRD spectra (red solid lines) was obtained by using CADEM: calculate X-ray diffraction of epitaxial multilayers.<sup>1</sup>

Additionally, the XRD diffractograms of SLs with 111 and 148 periods ( $S_4$  and  $S_5$ , respectively) are displayed **Figure S4**. These SLs were grown 30 cm away from the cathode centres with the deposition conditions identical to ones used for  $S_3$ .

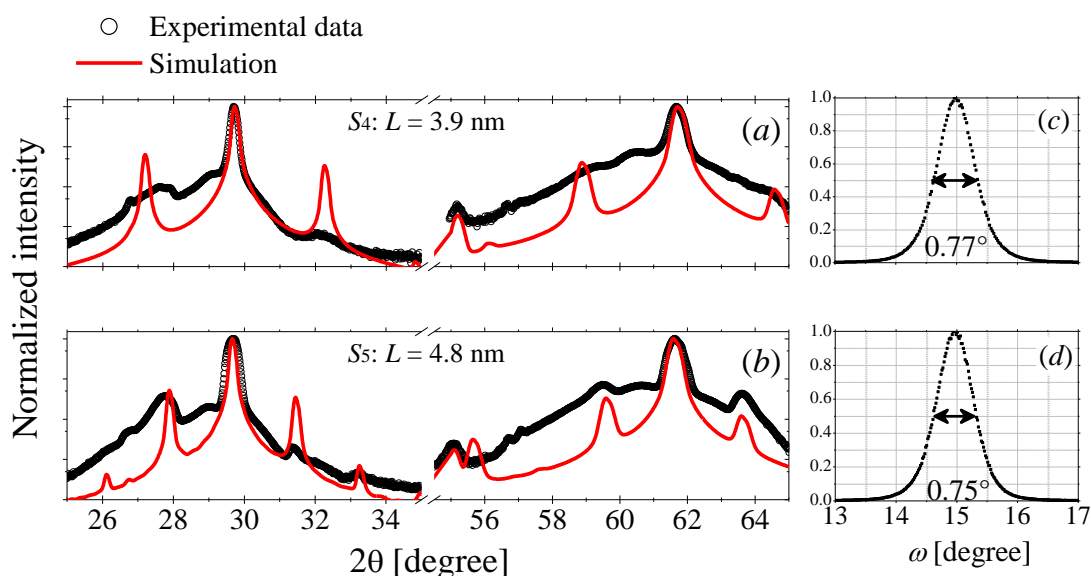


**Figure S4** XRD diffractograms (a) and (b), rocking curves (c) and (d) of 111 ( $S_4$ : a and c) and 147 ( $S_5$ : b and d) periods half-Heusler SLs grown under the same deposition conditions as for  $S_3$ . The best fitting theoretical diffractogram models are shown with red lines.<sup>1</sup>

## Supporting Information

As one can see in **Figure S4** the satellite peaks are weakly accented and the FWHM of the rocking curves decreases with increasing number of periods. That means that the epitaxial quality of the upper parts of the samples must be higher than the one of the lower parts. The period length in this case should be similar but one sees still shifts of the satellite peaks. The roughness rises significantly with the number of periods as one sees in the **Figure S5**.

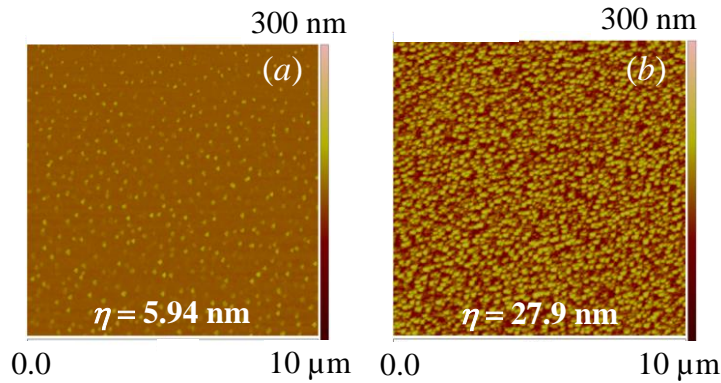


**Figure S5** AFM pictures of superlattices grown at high rate parameters in the inhomogeneous region containing: **(a)** 37,  $S_3$ , and **(b)** 111,  $S_4$ , periods, respectively.

Finally, the last set of samples was grown using the same conditions as for  $S_2$  but with larger number of periods  $N = 111$  ( $S_6$ ) in single sample holder and using a double sample holder ( $S_7$  and  $S_8$ ) keeping  $N = 37$ . In the double sample holder, there is room for two substrates lying side by side so that one substrate was closer to the HfNiSn cathode and the other to the TiNiSn cathode during deposition process. As the samples were grown in the inhomogeneous region, one of the SLs will contain more TiNiSn per period and the other will contain more HfNiSn per period.

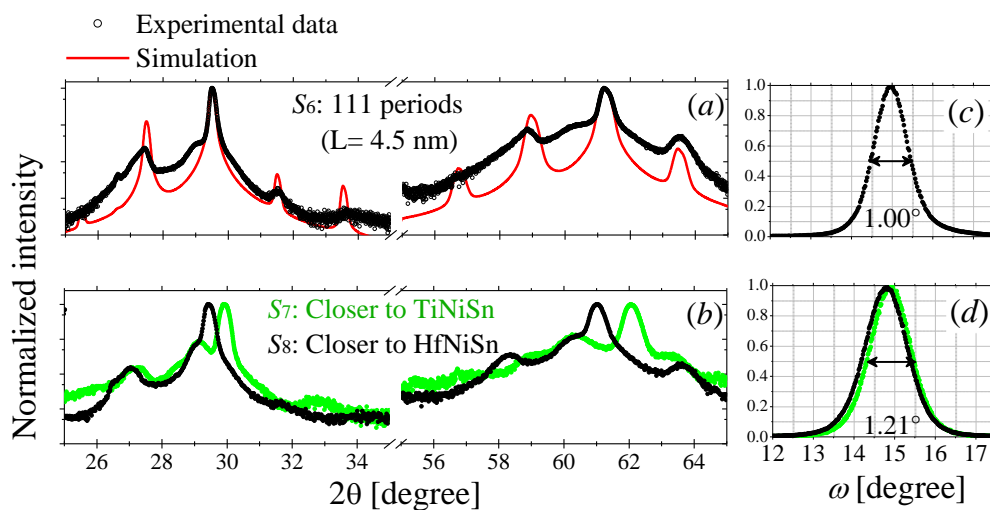


**Figure S6** XRD Diffractograms **(a)** and **(b)** and rocking curves **(c)** to **(d)** of 111 ( $S_6$ : **a** and **c**) and 37 ( $S_5$ : **b** and **d**) periods half-Heusler SLs grown under the same deposition conditions of  $S_2$ . The best fitting theoretical diffractogram models are shown with red lines.<sup>1</sup>

## Supporting Information

The period length of the samples measured here was determined from the best fit of the XRD using CADEM: calculate X-ray diffraction of epitaxial multilayers.<sup>1</sup> Open source and code software to calculate XRD diffractogram of any arbitrary multilayer structure. A summary of all the samples measured in this work is given in **Table S1**.

**Table S1** Summary of the deposition parameters, surface roughness, FWHM, and total thickness of investigated samples.

Parameter Sample	d [mm]	p [mbar]	P [W]		N	L [nm]	$\eta$ [nm]	FWHM [°]	Thickness [nm]	Sample holder
			TNS	HNS						
$S_1$	0	0.021	7	7	37	2.9	0.425	1.31	108	Single
$S_2$	30	0.021	7	7	37	3.5	0.906	1.53	107	Single
$S_3$	30	0.031	24	16	37	4.5	5.94	1.08	159	Single
$S_4$	30	0.031	24	16	111	3.9	27.9	0.77	450	Single
$S_5$	30	0.031	24	16	147	4.8	28	0.75	637	Single
$S_6$	30	0.021	7	7	111	4.5	-	1.00	506	Single
$S_7$	30	0.021	7	7	37	4.5	-	1.21	107	Double
$S_8$	30	0.021	7	7	37	4.5	-	1.21	107	Double

### 2. Three-omega method

The three-omega ( $3\omega$ ) method is an electrothermal technique widely used to determine the thermal conductivity of a specimen. The experiments are performed by inducing harmonic Joule heating in a narrow metal line ( $3\omega$ -heater), deposited onto the surface of the sample. The metallic strip acts simultaneously as a heater and thermometer due to its temperature dependent electrical resistance as it is displayed in **Figure S7 d**.

In our case, the  $3\omega$ -heater was patterned by photolithography and etching of a 50 nm thick gold thin film, grown in situ just after the deposition of  $\text{AlO}_x$  insulation layer. A schematic representation and a real picture of one the samples is displayed in **Figure S7 a** and **b**, respectively. The deposited metallic strip is composed of four rectangular pads connected by pins to the narrow heating wire. The width of the heating line is defined as  $2b = 20 \mu\text{m}$  and the length as  $l = 1 \text{ mm}$ , the latter being determined by the distance between the inner pads. The outer two pads are used to apply the AC electrical current that generates the Joule heating. The inner two pads are used to measure the voltage, which contains the third harmonic component. In the experiments, a sinusoidal electrical current is applied through the resistive strip as:

$$I_{app}(t) = I_0 \cos(\omega t) \quad (1)$$

where  $I_0$  is the amplitude of the signal.

## Supporting Information

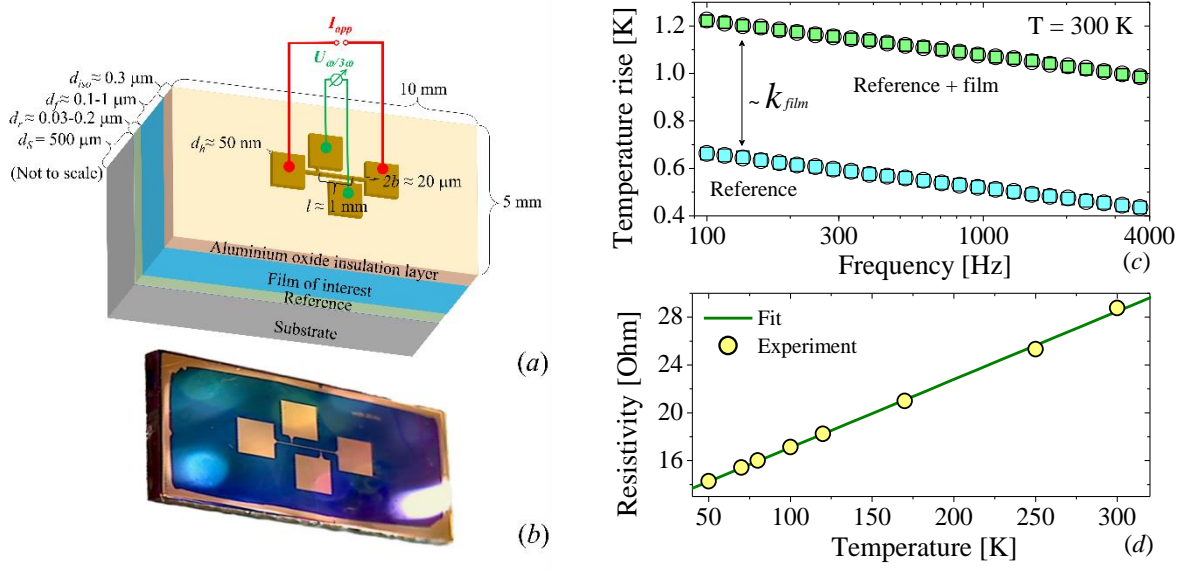


**Figure S7** (a) Schematic representation of the samples measured in this work and (b) real picture of one of them. (c) Temperature rise of  $3\omega$ -heater vs frequency of  $1000 \mu\text{m}$  thick HfNiSn thin film (green squares and empty dots) and its reference (blue square and empty dots). (d) Typical temperature dependence of the electrical resistivity of a  $3\omega$ -heater.

By Joule effect, this excitation results in power dissipation that consists of a DC and AC components given by:

$$P(t) = I_{app}(t)^2 R = \frac{I_0^2 R}{2} (1 + \cos(2\omega t)) \quad (2)$$

where  $R_0$  is the resistance of the strip. As the dissipated power has a DC and AC component, the heat dissipation will result in a temperature rise that has a DC ( $\Delta T_{DC}$ ) and an AC ( $\Delta T_{AC}$ ) component. The temperature fluctuation of amplitude  $\Delta T_{2\omega}$  will also oscillate at the same frequency.

$$T(t) = \Delta T_{DC} + \Delta T_{AC} \cos(2\omega t + \phi) \quad (3)$$

where  $\phi$  is the phase lag. Since the electrical resistivity is linearly proportional to the temperature (see **Figure S7 c**), the  $\Delta T$  will also produce a  $2\omega$  oscillation in the resistivity as:

$$R(T, t) \approx R_0 (1 + \beta \Delta T_{DC} + \beta \Delta T_{AC} \cos(2\omega t + \phi)) \quad (4)$$

where  $\beta$  is the temperature coefficient of the electrical resistivity of the strip. Now, by applying the Ohm's law, we obtain the modulation of the voltage of the form:

## Supporting Information

$$\begin{aligned}
 U &= R(T, t)I(t) \\
 &= I_0 R_0 \cos(\omega t) (1 + \beta \Delta T_{DC} + \beta \Delta T_{AC} \cos(2\omega t + \phi)) \\
 &= U_0 (1 + \beta \Delta T_{DC}) \cos(\omega t) + \frac{U_0 \beta \Delta T_{AC}}{2} (\cos(\omega t + \phi) + \cos(3\omega t + \phi))
 \end{aligned} \tag{5}$$

From (5), one is able to infer the temperature oscillations by measuring the voltage signal at the  $3\omega$  frequency<sup>2,3</sup>:

$$\Delta T_{AC} = \Delta T_{2\omega} = \frac{2U_{3\omega}}{\beta U_0} \approx \frac{2U_{3\omega, rms}}{\beta U_{\omega, rms}} \tag{6}$$

Since the  $3\omega$  response of the voltage is very small in comparison with  $1\omega$ , the lock-in technique is required to extract the signal. The thermal fluctuation can therefore be obtained from the  $3\omega$  component in terms of root mean square quantities (rms), as usually measured by lock-in amplifier. Due to the difference among  $1\omega$  and  $3\omega$  is several orders of magnitude, the noise of the whole  $1\omega$  signal is in the same order as the  $3\omega$  signal itself. To avoid this problem,  $U_{3\omega}$  is not measured directly at the inner pads of the heater but rather with a passive circuit.

The thermal conductivity can be obtained by solving the transient heat conduction equation for a finite width line heater, deposited onto semi-infinite surface of a film-on substrate system. The temperature rise is given by:

$$\Delta T_{2\omega} = \frac{P}{lk\pi} \int_0^{\infty} \frac{\sin^2(xb)}{(xb)^2 \sqrt{x^2 + q^2}} dx \tag{7}$$

where  $P$  is the applied power,  $q \equiv 1/\lambda = \sqrt{2\omega/\alpha}$  is the inverse of the thermal penetration depth ( $\lambda$ ),  $\alpha$  is the thermal diffusivity and  $k$  is the thermal conductivity of the material. The Eq. (7) does not have an analytical solution, however, Cahill<sup>2,3</sup> showed that for  $\lambda \gg b$  the heater can be seen as line source. Then, the upper limit of the integral can be replaced by  $1/b$  and the sinusoidal term goes  $\sin(xb)/(xb) \sim 1$  in the limit of  $b \rightarrow 0$ . By introducing these approximations, the analytical solution is given by:

$$\Delta T_{2\omega} = \frac{P}{2lk\pi} \left( -\ln(2\omega) + \ln\left(\frac{k}{\alpha b^2}\right) + 2\gamma \right) - \frac{iP}{4kl} \tag{8}$$

where  $\gamma$  is constant. Finally, the  $k$  can be extracted from the slope of the real part of temperature rise vs  $\ln(2\omega)$ :

## Supporting Information

$$k \approx \frac{P}{2\pi d} \left( \frac{d(\Delta T_{2\omega})}{d \ln(2\omega)} \right)^{-1} \quad (9)$$

This approximation of the  $3\omega$  measurement is known as slope method. In the following section the errors associated to the slope method are discussed and analyzed for our particular case. For an extended and detailed description on the derivation errors, mathematical expressions and the methodology used to calculate it, the readers are referred to the work of H.S. Carslaw and J.C. Jaeger<sup>4</sup>, D. Cahill<sup>2,3</sup>, Borca-Tasciuc et al.<sup>5</sup> C. Dames<sup>6</sup> and references therein.

### 2.1 Errors from mathematical description

There are three main requirements that the system has to hold to apply directly the slope method, those are: the heater is a line source, the substrate thickness is semi-infinite and the heater is infinitely long. As the real heater is not infinitesimal narrow and infinitely long in comparison to finite thick substrate. There are some limits where these considerations are valid and they are summarized in the Figure S8. As one can see in Figure S8, in our measurements, it is always possible to choose frequencies for the  $3\omega$  method to fulfil the criteria needed for the slope method, with errors below 5%.

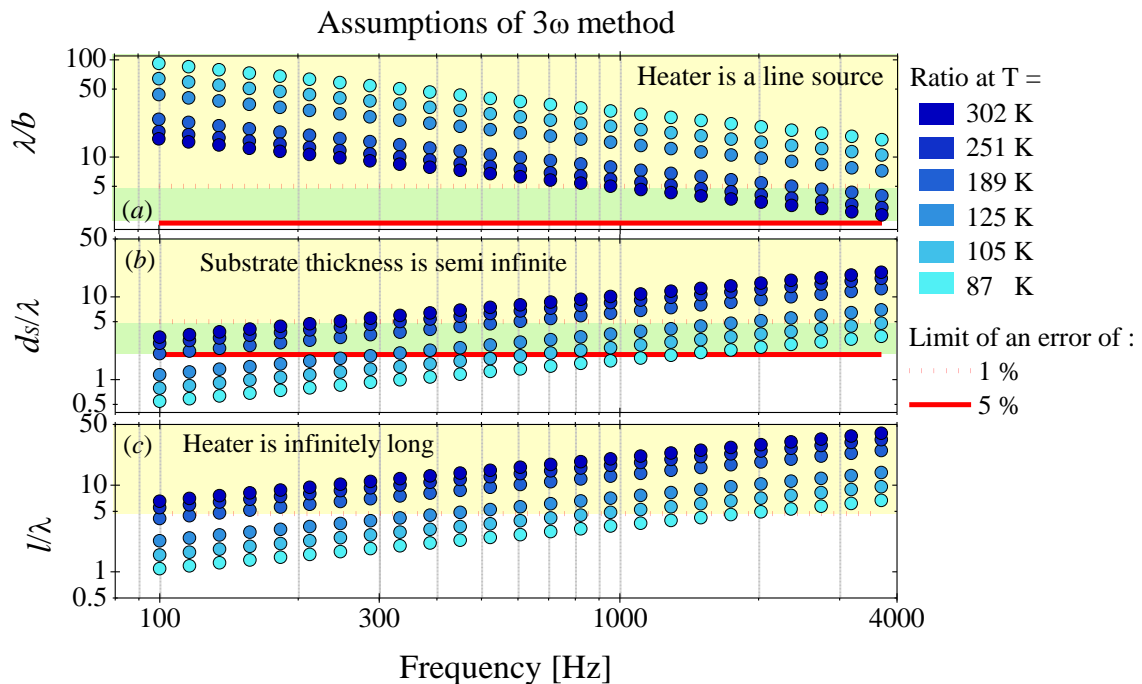


**Figure S8** Calculated ratios and criteria for the adequacy of the applied mathematical model for our  $3\omega$  measurements: (a) the heater is a line source, (b) the substrate thickness is infinite and (c) the heater line is infinitely long. A point fulfils a criteria if it is above the red lines in the yellow or green rectangle for an error below 1% and 5%, respectively. The substrate capacity and conductivity values that were needed to calculate the substrate penetration depth were taken from reference.<sup>7</sup> The criteria are taken from Ref.<sup>6</sup>.

## Supporting Information

### 2.2 Differential method: determination of the $k$ of a thin film

Once we ensure that the slope method can be applied in our substrates, the next step is calculation estimation of  $k$  of the film of interest by using the  $3\omega$  differential method.<sup>8,9</sup> In case of a film that has a conductivity much smaller than the substrate and a heater width that is larger than the film thickness, one can model the film as a frequency independent resistance where the bigger part of the heat flows cross plane from heater-film-interface to film-substrate-interface.<sup>8</sup> In this case the Fourier law can be applied in one dimension:

$$P = Q = kA_{\text{int}} \frac{\Delta T_f}{d_f} \approx 2klb \frac{\Delta T_f}{d_f} \quad (10)$$
$$\Rightarrow k = \frac{Pd_f}{2lb\Delta T_f}$$

where  $Q$  is the modulus of the heat flow,  $A_{\text{int}}$  is the area below the heater strip ( $A_{\text{int}} = 2lb$ ) and  $\Delta T_f$  is the temperature rise of the film. Since the  $3\omega$  measurement gives only the temperature difference oscillation amplitude between top (interface heater-sample) and bottom (interface of sample to the infinite sink) of the whole sample, it is not possible to measure  $\Delta T_f$  directly. But if one creates a film that consists not only of the film of interest but adds a small reference, the measurable quantity temperature rise of the system ( $\Delta T_{\text{sys}}$ ) can be super-posed by the  $\Delta T_f$  and the  $\Delta T_r$  of the system containing the substrate and the reference (see **Figure S7 a**). Then the temperature rise of the system can be expressed as:

$$\Delta T_{\text{sys}} = \Delta T_r + \Delta T_f \quad (11)$$

The  $\Delta T_r$  is obtained directly by measuring other sample that contains only the substrate and the reference film. Finally, the thermal conductivity of the film of interest is obtained by subtracting the  $\Delta T_{\text{sys}}$  and  $\Delta T_f$  and given by:

$$k = \frac{Pd_f}{2bl(\Delta T_{\text{sys}} - \Delta T_r)} \quad (12)$$

Therefore, for each film-on-substrate measurement, it is required to create and measure at least two samples, namely one sample containing the film of interest as well as a reference part and a second sample containing only the reference part (see **Figure S7 c**). Naturally both reference parts need to be created under similar conditions on equal substrates. In our case the reference consisted of 5 nm of vanadium and 25 nm of HfNiSn buffer layers. It is important to mention that as the width of the heater line is not exactly the same in each sample, a correction of the  $\Delta T$  must to be applied as follows:

## Supporting Information

$$\Delta T_c = \frac{b_{mask}}{b_{measured}} \Delta T = c_b \Delta T \quad (13)$$

The correction takes into account the deviation in heater width due to the photolithographic processes. This quantity was estimated through image analysis of five pictures taken with an optical microscope using a 100x objective along of the  $3\omega$ -strip.

To perform a  $T$  measurement with this method, one needs to create a difference of  $T$  without a significant  $\Delta T$  in the substrate. The error given by this simplification is less than 1%, if the ratio  $(k_f/k_s)^2 < 0.01$ . In our case all observed  $k_f < 5$  W/(K m) and the lowest observed  $k_s \approx 50$  W/(K m), then, this criteria is fulfilled for all measurements.<sup>6</sup> The error propagation for the differential method leads to errors about 5%, a mathematical error in this range is tolerable here and the line source criteria does not need to be fulfilled as strictly as for the slope method. To achieve an error lower than 5% the ratio  $\lambda/b \leq 2.1$  and for an adequate semi-infinite substrate assumption  $d_s/\lambda$  must be bigger than two. The complete requirements for these approximations are shown in **Figure S8**.

### 2.3 Estimation of measurement errors for thin film measurements

For the measurements done in this work, it was always tried to keep the errors caused by the mathematical model as low as possible by choosing an adequate frequency range for present environment temperature. Therefore, the line source assumption and the semi-infinite substrate assumption were taken into account as well as the infinitely long heater assumption. It is not possible to find a range where all limits for an error lower than 1% are fulfilled at the same time for all the temperatures. One reason for this is the fact that the line source criterion behaves in a different way as a function of temperature than the other two criteria. But we can be sure, that the errors caused by mathematical assumptions are always below 5%.

## Supporting Information

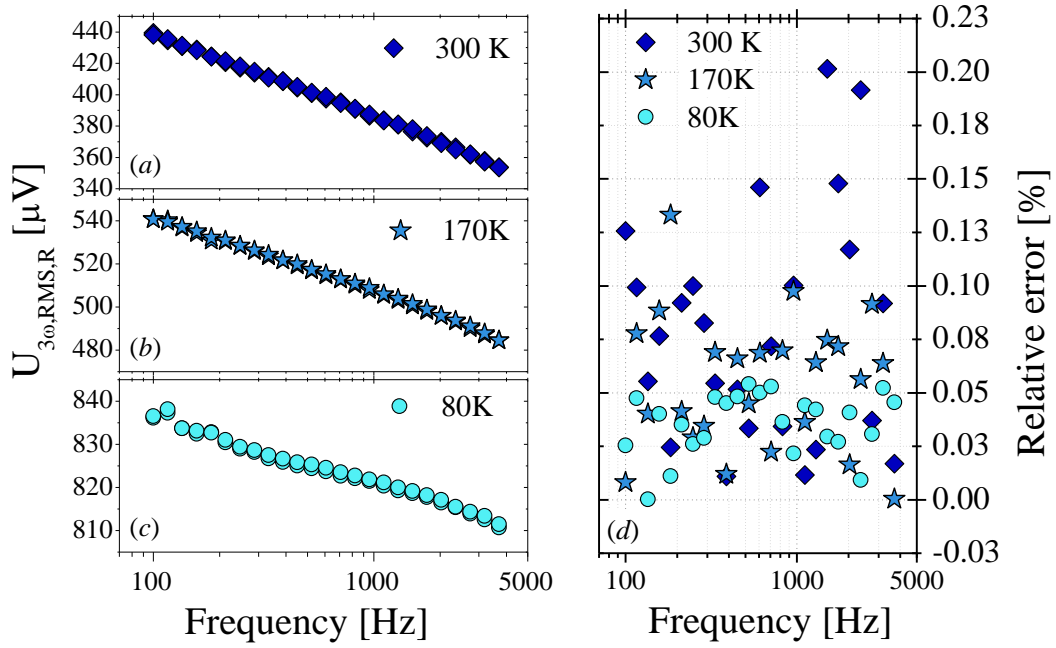


**Figure S9** Measured three omega voltages (a) to (c) and relative error (d) at each frequency for  $1\mu\text{m}$  thick HfNiSn thin film at three different temperatures  $T = 300$  (a),  $170$  (b) and  $80$  (c) K for fixed power  $P = 20\text{ mW}$ . The estimations done by the mathematical model are not the only possible sources of errors. The  $3\omega$ -method requires several measurements of electrical and geometrical quantities that contain statistical errors that will affect the result as shown in **Table S2** and **Table S3**.

**Table S2** Relative errors of the measured electrical quantities of the used  $3\omega$ -method. The errors for  $R_0$  and  $P$  can be calculated with this values using error propagation.

$\delta_{rel} dR/dT$	$\delta_{rel} U_{\omega,RMS}$	$\delta_{rel} I_{\omega,RMS}$	$\delta_{rel} U_{3\omega,RMS}$
0.5 %	0.1 %	0.1 %	0.3 %

In contrast to the other measured quantities, the determination of the third omega signal  $U_{3\omega,RMS}$  is not straightforward. Therefore one needs to explain how the errors are determined in this case. For each sample at each measured temperature, the chosen frequency range is measured at least twice. The error was determined by the deviation of both measured points. An example for this praxis is showed in **Figure S9**. The deviation of a point at each frequency leads to relative errors less than 0.2% in this example. The highest relative error of  $U_{3\omega,RMS}$  measured in this work was 0.3%.

**Table S3** Relative errors of the measured geometrical quantities of the used  $3\omega$ -method.

$\delta_{rel} d_f$	$\delta_{rel} l$	$\delta_{rel} b$	$\delta_{rel} c_b$
2.0 %	0.5 %	Expressed in $c_b$	1.0 %

The propagation of uncertainty is done below for the absolute error  $\delta x$  of the general quantity  $x$ . The single quantities are assumed as uncorrelated. As an example, the error propagation for the temperature coefficient of the resistance  $\beta$  is calculated below:

## Supporting Information

$$\delta\beta = \sqrt{\left(\frac{\delta dR/dT}{R_0}\right)^2 + \left(\frac{\delta R_0 dR/dT}{R_0^2}\right)^2} \quad (14)$$

The error propagation for the corrected temperature oscillation amplitude  $\delta\Delta T_c$  can be written as:

$$\delta\Delta T_c = 4 \left[ \frac{c_b^2 \delta U_{\omega,RMS}^2 U_{3\omega,RMS}^2}{\beta^2 U_{\omega,RMS}^4} + \frac{c_b^2 \delta\beta^2 U_{3\omega,RMS}^2}{\beta^4 U_{\omega,RMS}^2} + \frac{c_b^2 \delta U_{\omega,RMS}^2}{\beta^2 U_{\omega,RMS}^2} + \frac{\delta c_b^2 U_{3\omega,RMS}^2}{\beta^2 U_{\omega,RMS}^2} \right]^{1/2} \quad (15)$$

The error propagation for the  $k$  of the differential method can be expressed as:

$$\delta k = \left[ \frac{d_f^2 \delta l^2 P^2}{4b^2 l^4 (\Delta T_{sys,c} - \Delta T_{r,c})^2} + \frac{d_f^2 \delta \Delta T_{r,c}^2 P^2}{4b^2 l^2 (\Delta T_{sys,c} - \Delta T_{r,c})^4} + \frac{d_f^2 \delta \Delta T_{sys,c}^2 P^2}{4b^2 l^2 (\Delta T_{sys,c} - \Delta T_{r,c})^4} + \frac{d_f^2 \delta P^2}{4b^2 l^2 (\Delta T_{sys,c} - \Delta T_{r,c})^4} + \frac{\delta d_f^2 P^2}{4b^2 l^2 (\Delta T_{sys,c} - \Delta T_{r,c})^2} \right]^{1/2} \quad (16)$$

Due to the mathematical expressions for  $\beta$  and  $\Delta T_c$  only contain products, the relative errors  $\delta_{rel}x = \delta x/x$  can be expressed as:

$$\delta_{rel}\beta = \frac{\delta\beta}{\beta} = \sqrt{(\delta_{rel} dR/dT)^2 + (\delta_{rel} R_0)^2} \quad (17)$$

$$\delta_{rel}\Delta T_c = \frac{\delta\Delta T_c}{\Delta T_c} = \sqrt{(\delta_{rel} c_b)^2 + (\delta_{rel} U_{\omega,rms})^2 + (\delta_{rel} U_{3\omega,rms})^2 + (\delta_{rel} \beta)^2} \quad (18)$$

One sees here, that the relative error of  $\Delta T_c$  depends only on the relative errors of measurement instruments. Usually, it is possible to assume that the relative error of an instrument only depends on the chosen measurement scale. Then, if one uses the same scale for each measured sample, the relative error does neither depend on the single measured value of a quantity nor on the measured sample. Therefore, we can assume that the relative error  $\delta_{rel}\Delta T_c$  is constant for each measurement. The case is different for the  $k$ , because,  $k$  contains the difference  $(\Delta T_{sys,c} - \Delta T_{r,c})$ , thus it cannot be expressed just in terms of relative errors and therefore does not stay constant. But, the largest part of it can be expressed with relative measurement errors, so that it shows only a dependence on the ratio  $\Delta T_{sys,c}/\Delta T_{r,c}$ :

## Supporting Information

$$\delta_{rel}k = \frac{\delta k}{k} = \left[ (\delta_{rel}d_f)^2 + (\delta_{rel}l)^2 + (\delta_{rel}P)^2 + (\delta_{rel}\Delta T_{r,c})^2 (\Delta T_{sys,c} / \Delta T_{r,c} - 1)^{-2} + (\delta_{rel}\Delta T_{sys,c})^2 (1 - (\Delta T_{sys,c} / \Delta T_{r,c})^{-1})^{-2} \right]^{1/2} \quad (19)$$

In **Figure S10** this function is plotted for the instrument errors shown in **Table S2** and **Table S3**. Notice that the relative error of  $k$  decreases with increasing  $\Delta T_{sys,c}/\Delta T_{r,c}$ . Therefore, it is advisable to grow samples with a thickness difference between reference and film of interest as large as possible. In this way it is warranted that the  $\Delta T$  ratio is large enough. It is important to notice that the  $\Delta T_{sys,c}/\Delta T_{r,c}$  is also dependent on the difference of  $k$  between reference and film of interest, then, it will not be similar for samples with equal thickness. In our work the  $\Delta T_{sys,c}/\Delta T_{r,c}$  is close to 1.5 for most of the samples measured in this work. This leads to errors between 4 and 7%.

For all the measurements carried out in this work, at least two measurement points of  $U_{3\omega,rms}$  were taken for similar conditions of the same sample (See **Figure S7 c**). In this way, one can see statistical deviations as well as the errors calculated with error propagation. This statistical deviations are much smaller than the error bars calculated with the Eq. (19), because they only depend on deviations of  $U_{3\omega,rms}$  while the error propagation takes several additional error sources into account. Therefore the error propagation is more feasible than considering simply the statistical errors of  $U_{3\omega,rms}$ .

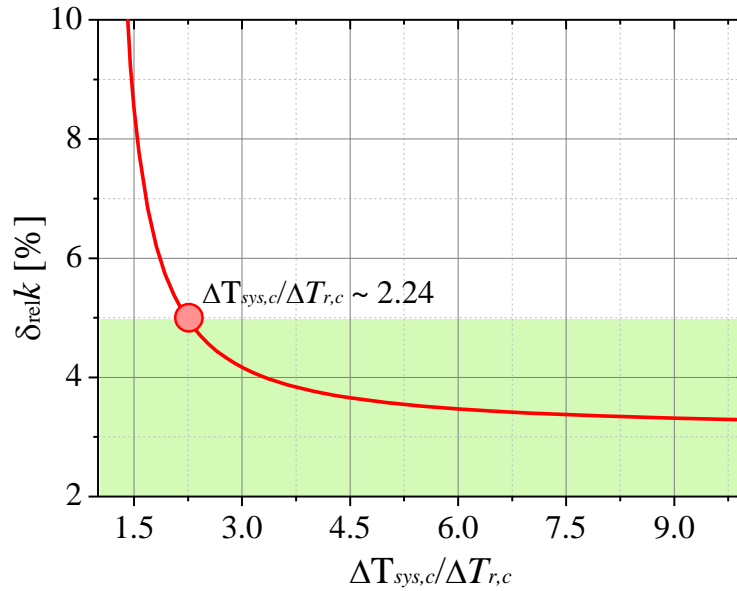


**Figure S10** Relative error of the thermal conductivity for the differential method in dependence of the ratio  $\Delta T_{sys,c} / \Delta T_{r,c}$ . The curve is dependent on the relative errors of the measured quantities. This curve was calculated for the estimated errors of the  $3\omega$  setup used in this work.

## Supporting Information

### 3 Calculation of amorphous limit of the thermal conductivity

The lowest thermal conductivity value for semiconductors and insulating materials is achieved for the systems with the small order what is similar to the amorphous state. The pioneer theoretical framework on heat conduction in amorphous materials was first proposed by Einstein<sup>10</sup>, refined by Slack<sup>11</sup> and extended by Cahill et al.<sup>12</sup> The theory is basically based on the assumption of that heat conduction is described by a “random walk” of independent oscillators with a characteristic frequency (Einstein frequency). Then, each atom is coupled to its first-, second-, and third nearest neighbors on a simple cubic lattice by harmonic forces. Slack reformulated this problem by considering that the minimum MFP ( $\Lambda$ ) of a heat carrier has to be the same as its wavelength ( $\lambda$ ), namely  $\Lambda = \lambda$ .<sup>11</sup> The  $k$  estimated by this model is known as the minimum thermal conductivity or amorphous limit ( $k_{\min}$ ). Following both works, Cahill *et al.*<sup>12</sup> further extended this model by dividing the system into regions of size  $\lambda/2$ , with a constant velocity given by the Debye speed of sound. Then, the  $\Lambda$  of each oscillator is assumed to be  $\lambda/2$ . Finally, the  $k$  is reformulated in terms of sum of three Debye integrals as follows<sup>12</sup>:

$$k_{\min} = \left(\frac{\pi}{6}\right)^{1/3} k_B n^{2/3} \sum_j v_j \left(\frac{T}{\Theta_{D,j}}\right)^2 \int_0^{\Theta_{D,j}/T} \frac{x^3 e^x}{(e^x - 1)^2} dx \quad (20)$$

where  $\sum_j$  represents the sum on longitudinal ( $L$ ) and transverse ( $T$ ) polarizations,  $n$  is the number density of atoms (i.e.,  $n = \text{number of atoms in a unit cell} / \text{volume of unit cell}$ ),  $k_B$  is the Boltzmann constant,  $\Theta_{D,i}$  is the Debye temperature given by:

$$\Theta_{D,i} = \frac{h v_i}{2\pi k_B} (6\pi^2 n)^{1/3} \quad (21)$$

where  $h$  is the Planck constant. The **Table S4** summarizes all the parameters used in this work to calculate the amorphous limit of the HH compounds.

**Table S4** Parameter used to estimate the amorphous limit of the thermal conductivity of the HHs compounds.

Parameter	TiNiSn	HfNiSn
$v_L$	5952 [m/s] <sup>13</sup>	4195 [m/s] <sup>14</sup>
$v_T$	3427 [m/s] <sup>13</sup>	2783 [m/s] <sup>14</sup>
$a$	0.5941 [nm] <sup>15</sup>	0.6083 [nm] <sup>16</sup>
Number of atoms per unit cell	12	12

## Supporting Information

The amorphous limit of the effective material was calculated as the reciprocal of the average of the minimum thermal conductivities. The temperature dependence of the amorphous limit for each compound is displayed in **Figure S11**.

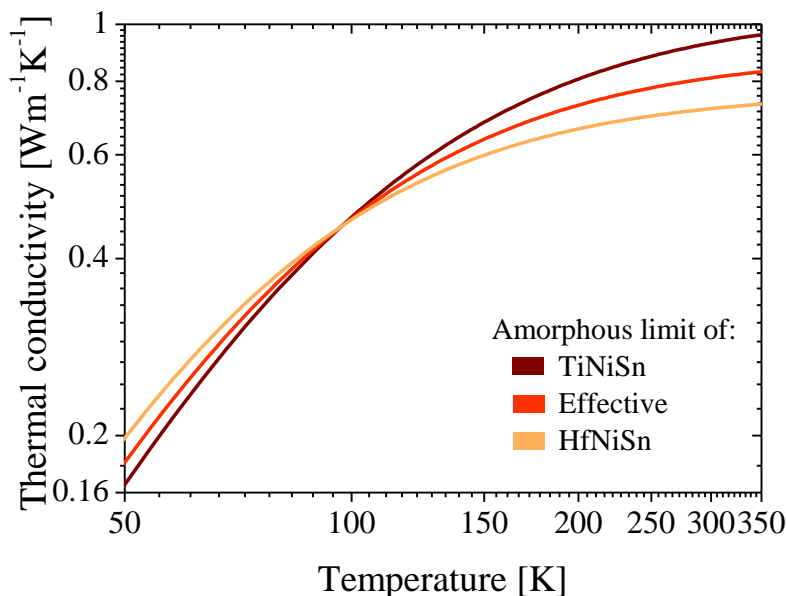


**Figure S11** Amorphous limit of the different HH compounds and the effective material.

## References

- (1) Komar, P.; Jakob, G. CADEM : Calculate X-Ray Diffraction of Epitaxial Multilayers. *J. Appl. Crystallogr.* **2017**, *50* (1), 288–292.
- (2) Cahill, D. G. Thermal Conductivity Measurement from 30 to 750 K: The  $3\omega$  Method. *Rev. Sci. Instrum.* **1990**, *61* (2), 802.
- (3) Cahill, D. G. Erratum: “Thermal Conductivity Measurement from 30 to 750 K: The  $3\omega$  Method” [Rev. Sci. Instrum. 61, 802 (1990)]. *Rev. Sci. Instrum.* **2002**, *73* (10), 3701.
- (4) Carslaw, H. S. ; Jaeger, J. C. . The Flow of the Heat in an Infinite Circular Cylinder. In *Conduction of Heat in Solids*; Oxford University Press: London, 1959; pp 188–214.
- (5) Borca-Tasciuc, T.; Kumar, A. R.; Chen, G. Data Reduction in  $3\omega$  Method for Thin-Film Thermal Conductivity Determination. *Rev. Sci. Instrum.* **2001**, *72* (4), 2139–2147.
- (6) Dames, C. Measuring the Thermal Conductivity of Thin Films: 3 Omega and Related Electrothermal Methods. *Annu. Rev. Heat Transf.* **2013**, *16* (1), 7–49.
- (7) Cahill, D. G. . Thermal conductivity bulk single crystal MgO; Temperature dependence of volumetric heat capacity MgO. Department of Materials Science and Engineering. University

## Supporting Information

of Illinois at Urbana Campaign <http://users.mrl.illinois.edu/cahill/tcdata/tcdata.html> (accessed Jan 1, 2016).

- (8) Cahill, D.; Katiyar, M.; Abelson, J. Thermal Conductivity of a-Si:H Thin Films. *Phys. Rev. B* **1994**, *50* (9), 6077–6081.
- (9) Kim, J. H.; Feldman, A.; Novotny, D. Application of the Three Omega Thermal Conductivity Measurement Method to a Film on a Substrate of Finite Thickness. *J. Appl. Phys.* **1999**, *86* (7), 3959–3963.
- (10) Einstein, A. Elementare Betrachtungen Über Die Thermische Molekularbewegung in Festen Körpern. *Ann. Phys.* **1911**, *340* (9), 679–694.
- (11) Slack, G. A. The Thermal Conductivity of Nonmetallic Crystals. In *Solid State Physics Vol. 34*; Ehrenreich, H., Seitz, F., Turnbull, D., Eds.; Academic Press: New York, San Francisco & London, 1979; pp 1–71.
- (12) Cahill, D. G.; Watson, S. K.; Pohl, R. O. Lower Limit to the Thermal Conductivity of Disordered Crystals. *Phys. Rev. B* **1992**, *46* (10), 6131–6140.
- (13) Hichour, M.; Rached, D.; Khenata, R.; Rabah, M.; Merabet, M.; Reshak, A. H.; Bin Omran, S.; Ahmed, R. Theoretical Investigations of NiTiSn and CoVS<sub>n</sub> Compounds. *J. Phys. Chem. Solids* **2012**, *73* (8), 975–981.
- (14) Özisik, H.; Çolakoglu, K.; Özisik, H. B. Ab-Initio First Principles Calculations on Half-Heusler NiYSn (Y=Zr, Hf) Compounds Structural, Lattice Dynamical and Thermodynamical Properties. *AJP Fiz.* **2010**, *16* (2), 154–157.
- (15) Romaka, V. V.; Rogl, P.; Romaka, L.; Stadnyk, Y.; Melnychenko, N.; Grytsiv, A.; Falmbigl, M.; Skryabina, N. Phase Equilibria, Formation, Crystal and Electronic Structure of Ternary Compounds in Ti–Ni–Sn and Ti–Ni–Sb Ternary Systems. *J. Solid State Chem.* **2013**, *197*, 103–112.
- (16) Larson, P.; Mahanti, S. D.; Kanatzidis, M. G. Structural Stability of Ni-Containing Half-Heusler Compounds. *Phys. Rev. B* **2000**, *62* (19), 12754–12762.